Morphological response to a North Sea bed depression induced by gas mining

Caroline C. J. M. Fluit and Suzanne J. M. H. Hulscher
Department of Civil Engineering, University of Twente, Enschede, Netherlands

Received 15 February 2001; revised 26 July 2001; accepted 3 October 2001; published 26 March 2002.

[1] Gas mining leads to saucer-like surface depressions. In the North Sea, gas is currently mined at several offshore locations. The associated bed depression has a similar spatial extent as offshore tidal sandbanks, which are large-scale bed patterns covering a significant part of the North Sea bottom. The morphological time scales of bed depressions and tidal sandbanks are similar, so that significant interaction between these features is expected. In this paper we allow the bed depression to become morphologically active. A simple depression model based on a homogeneous soil is tuned with data of a bed depression near the Dutch barrier island of Ameland. Next, this subsidence model is included in a morphodynamic model. We show that this model is able to explain tidal sandbanks, which represent natural bed behavior. Here we approximate the solution by an expansion up to first order. The zeroth-order solution of the model is a flat bed with a spatially uniform, time-independent current. The first-order solution is investigated using a Fourier transformation. In general, we observe significant interaction between the bed depression and the natural sandbank formation process. The process of induced bed depression triggers and intensifies the natural morphological behavior of the offshore seabed. The model also shows essential differences between modeling a morphodynamically active marine bottom depression and a bottom depression below the threshold for sediment motion. The maximum bed level depression in the active case is significantly larger, and the circular shape of depression contours is affected by stretching toward the preferred orientation of the tidal sandbank formation process. *INDEX TERMS:* 3045 Marine Geology and Geophysics: Seafloor morphology and bottom photography; 3200 Mathematical Geophysics; 3210 Mathematical Geophysics: Modeling; 4560 Oceanography: Physical: Surface waves and tides (1255); *KEYWORDS:* sandbanks, gasmining, morphology, offshore, bed depression, morphodynamics

1. Introduction

[2] Gas mining leads to a decrease of pore pressure in the reservoir rock (such as sandstone) and hence compression. In the case of offshore drilling the overlying seabed consequently subsides, and if the seabed is sandy, regular processes of sediment transport may gradually deform such a depression.

[3] Observations of the topographies of marine beds mined for gas and their long-term evolution are not available. In this paper we therefore model seabed evolution in response to gas mining, taking into account sediment mobility due to water motion. Thus we can assess whether there are essential differences between modeling the evolution of a marine bottom depression and a depression below the threshold of sediment motion.

[4] Gas drilling is carried out in the North Sea and the Wadden Sea, for example, near the Dutch island of Ameland. Without sediment transport the sea bottom subsides into a more or less circular bottom depression with a characteristic smooth saucer shape. The cross-sectional shape changes from convex to concave. The locus of the inflection points forms approximately a circle; the radius is called the horizontal bed depression. In the Ameland case the cross section of the bottom depression, partly on the island and partly on the seabed, is about 8 km [*Eysink et al.*, 1995]. This depression is of approximately the same size as the tidal sandbanks (Figure 1), which are also observed in this area.

[5] Tidal sandbanks form large-scale regular patterns on the bed of shallow coastal seas, like the North Sea. The crests' spacing is 5–10 km. The crests (troughs) can reach up to 20 m above (below) the mean bed level, which is very high compared to the water depth in shallow seas (e.g., 30 m) [*Hulscher and van den Brink*, 2001; *Knaapen et al.*, 2001, and references therein]. *Dyer and Huntley* [1999] recently reviewed the characteristics and formation processes of tidal sandbanks. The tidal currents must be strong: 0.5–2.3 m s^{-1} [*Allen*, 1968] and tidal sandbanks' crests are oriented between 5° and 30° counterclockwise with respect to the principal current direction (Figure 2).

[6] Offshore tidal sandbanks can be formed by the interaction of topography and (tidal) currents, as *Huthnance* [1982] first showed. The driving mechanism originates from the interaction between the bottom friction and the spatial acceleration of the flow. In the Northern Hemisphere the Coriolis effect leads to a preference for a counterclockwise orientation with respect to the main axis of the tidal current ellipse [*Hulscher et al.*, 1993].

[7] In this study we allow sediment to be transported by a time-independent current. We also combine bed depression dynamics with morphological behavior. As we want to focus on the main mechanisms of seabed behavior, we use an idealized model so that analytical solutions can be obtained.

[8] The paper is structured as follows. In section 2 an empirical model of the bottom subsidence is derived. In section 3 this model is added to the depth-averaged shallow water equations, supplemented with a bottom evolution equation and a parameterization of the sediment transport. Section 4 discusses the solution concept, and section 5 presents the results. Section 6 gives the overall conclusions and final remarks.

0148-0227/02/2001JC000851$09.00

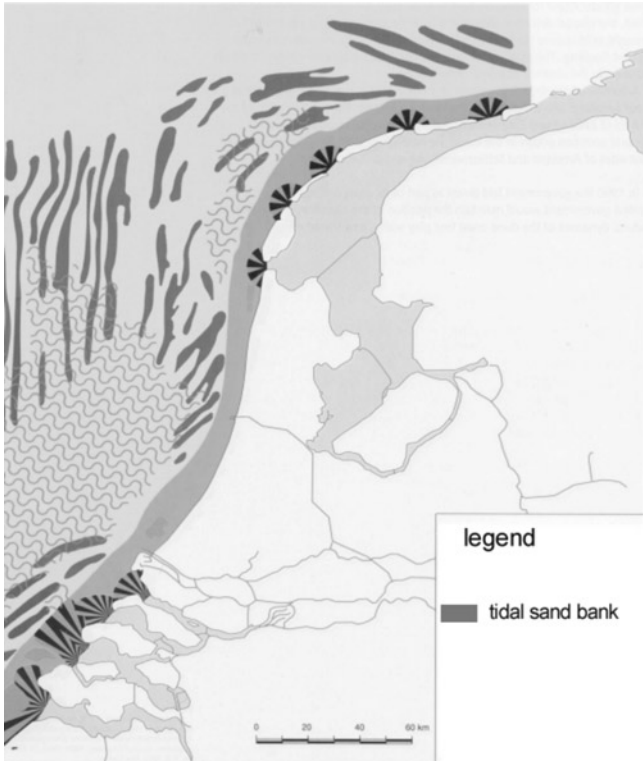

Figure 1. Location of tidal sandbanks and sand waves in the North Sea. Adapted after *Van Alphen and Damoiseaux* [1989]. See color version of this figure at back of this issue.

2. Bed Subsidence: Data Analysis and Model

[9] The Ameland gas field, the center of which is located at a depth of 3400 m, was discovered in 1964. Gas extraction started in 1986 via six wells located on the island of Ameland. The bottom subsidence on land, caused by this gas extraction has been monitored from October 1986. These measurements have a vertical accuracy of millimeters. Subsidence measurements at sea, which are much less accurate and difficult to perform, have not been carried out. Seven measurements of the bottom depression at Ameland are available, covering a period of 7 years (Figure 3). We use these Ameland data to create a three-dimensional (3-D) empirical model of the bed subsidence.

[10] To arrive at a 3-D mathematical description of the cross section of the bottom depression, a 1-D empirical model for bottom subsidence in soil mechanics is used in which the cross section of the bottom subsidence is described by [*Peck*, 1969]

$$\delta(x,t) = \delta_{\max}(t) e^{-\frac{x^2}{2R(t)^2}}. \tag{1}$$

Here the x axis is a horizontal reference line at the surface, t is time, and $\delta(x, t)$ is the negative surface deviation. The work of *Fluit* [1999], who investigated this approximation for the Ameland bottom depression data in detail, confirms that the Gaussian shape fits the observations best.

[11] The local subsidence, measured at three monitoring locations, is plotted against time (months after the start in October 1986) in Figure 4. This shows that the local subsidence increases almost linearly in time. The proportionality constant $\partial\delta(t)/\partial t$ can be approximated quite well by a constant, which differs for the three locations as they lie at different distances from the center. For all three locations the largest deviation was observed in month 39 (January 1990): the observed subsidence is stronger than linear. The reason for this systematic deviation is unknown (e.g., no changes in gas exploration). However, the deviation is not significant, and we can still conclude that the subsidence at each measurement location is linear in time. On the basis of this we estimate the subsidence speed at the depression center by $\partial\delta(t)/\partial t = \rho = 5.8 \times 10^{-10}$ m s^{-1}.

[12] Two parameters R and $\delta_{\max}$, which can both vary in time, determine the geometry of the bottom depression. R is the radius of the inflection circle inside the bottom depression and thus a measure for the horizontal dimension; $\delta_{\max}$ is the maximum subsidence in the center. The values of R and $\delta_{\max}$ are assumed to be mutually independent. The dynamical behavior of the bottom can be found from differentiating (1) with respect to time:

$$\frac{\partial\delta(x,t)}{\partial t} = \underbrace{e^{-\frac{x^2}{2R(t)^2}} \frac{\partial\delta_{\max}(t)}{\partial t}}_{\text{I}} + \underbrace{\delta_{\max}(t) e^{-\frac{x^2}{2R(t)^2}} \frac{x^2}{R(t^3)} \frac{\partial R}{\partial t}}_{\text{II}}. \tag{2}$$

Equation (2) contains two terms, i.e., (I) and (II), the magnitude of which can be estimated from the measured data.

[13] For the estimation of term (II) in (2) we study the temporal evolution of R. We approximate the observed bed deviation by the Gaussian shape function, (1), for three points in time. The result for the largest subsidence is shown in Figure 5. This gives an estimate for the radius R at these three points; see Table 1.

[14] These three points show that in contrast to $\delta_{\max}$, R does not increase monotonously and term (II) in (2) is significantly smaller than term (I). (For the period 1991–1994 the order of magnitude of R in (2) is estimated at 2.8×10^{-11} m s^{-1} (for 1991–1992 it amounts to -6.7×10^{-11} m s^{-1}).) This means that term (II) in ((2)) can be neglected with respect to term (I) and the radius of the bed subsidence is R = 3.0 km. Combining these conclusions with the assumption that the depth contours of a depression form circles around the center of the depression (x_d, y_d), which is reasonable for a uniform noncohesive soil, we find the following 3-D subsidence model:

$$\frac{\partial\delta(x,y,t)}{\partial t} = -\rho e^{-\frac{(x-x_d)^2+(y-y_d)^2}{2R^2}}. \tag{3}$$

3. Morphological Model Formulation

[15] This section considers a morphological model that describes the interaction between flow and an erodible bed in a shallow sea influenced by subsidence. We use a simple model, based on *Hulscher et al.* [1993], because we are mainly interested in the basic interaction of the depth-integrated tidal currents, the existing large-scale bed forms, and the bottom depression. The bottom evolution equation is extended with a subsidence term, which represents the bottom subsidence. We use the model for the

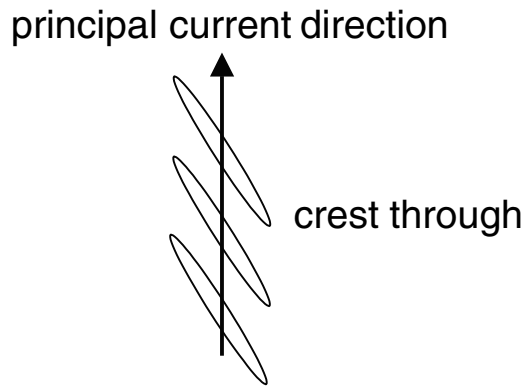

Figure 2. Sketch of the orientation of the tidal sandbanks if the orientation is approximately 30° counterclockwise with respect to the principal current direction.

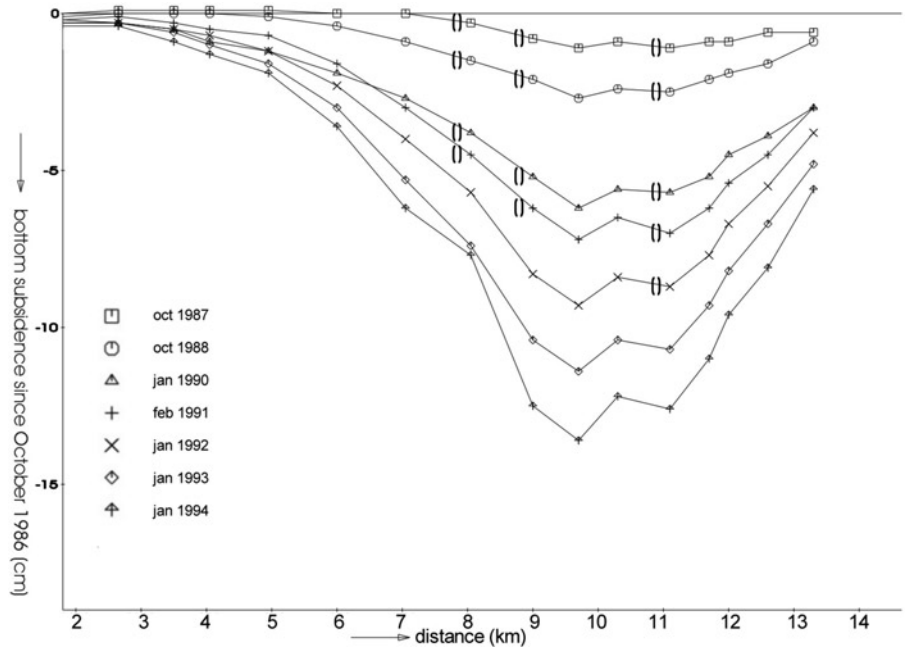

Figure 3. Bottom depression at Ameland measured from October 1986 until January 1994. The horizontal axis gives the distance (in kilometers) from a fixed Ameland location; the vertical axis denotes the subsidence (in centimeters) since October 1986. The parentheses indicate renaming of a measurement location. The data source is *Eysink et al.* [1995].

bottom subsidence described in section 2 to specify this term. In the morphodynamic model we have localized the center of the depression, $\mathbf{x}_d$ at the origin ($\mathbf{0}$) without any loss of generality. The resulting model reads:

$$\frac{\partial u}{\partial t}+u\frac{\partial u}{\partial x}+v\frac{\partial u}{\partial y}-fv=-g\frac{\partial \zeta}{\partial x}-r\frac{u}{H-h+\zeta}, \tag{4}$$

$$\frac{\partial v}{\partial t}+u\frac{\partial v}{\partial x}+v\frac{\partial v}{\partial y}+fu=-g\frac{\partial \zeta}{\partial y}-r\frac{v}{H-h+\zeta}, \tag{5}$$

$$\frac{\partial(\zeta-h)}{\partial t}+\frac{\partial}{\partial x}[(H+\zeta-h)u]+\frac{\partial}{\partial y}[(H+\zeta-h)v]=0, \tag{6}$$

$$\frac{\partial h}{\partial t}=-\nabla\cdot\mathbf{S}_b-\rho e^{-\frac{x^2+y^2}{2R^2}}, \tag{7}$$

$$\mathbf{S}_b=\alpha|\mathbf{u}|^b\left(\frac{\mathbf{u}}{|\mathbf{u}|}-\lambda\nabla h\right), \tag{8}$$

with

$$\nabla=\left(\frac{\partial}{\partial x},\frac{\partial}{\partial y}\right).$$

[16] Here u and v are the velocity components in the x and y direction, ζ indicates the free surface, and h indicates the bed topography with respect to the undisturbed bed level $z = -H$ (see also Figure 6). The sediment motion is described by $\mathbf{S}_b$. The x axis is chosen in the direction of the principal tidal current. Furthermore,

f Coriolis parameter;
α proportionality constant (includes the effect of porosity);
g acceleration due to gravity;
b power of sediment transport (usually 3–5);
r linearized friction parameter;
λ downhill constant (usually 1–3).

The tidal flow model is composed of three parts: a momentum balance of the flow motion in the x direction (equation (4)) and the y direction (equation (5)) and a mass balance for the water (equation (6)). No wind stress at the sea surface is assumed, and the shear stress at the bottom depends linearly on the mean flow velocity, which applies for tidal flow without wave effects, i.e., at depths larger than 20 m [*Zimmerman*, 1980]. *Komarova and Hulscher* [2000] have shown that such a model describes tidal motion well above the threshold value, which is about 0.3 m s^{-1} for the North Sea.

[17] The sediment balance (equation (7)) combines sediment transport $\mathbf{S}_b$ and a subsiding bottom and leads to the evolution equation for the seabed. Note that the model describing the subsidence dynamics (equation (3)) assumes a homogeneous, noncohesive soil composition. Though highly idealized, this model does describe the main characteristics of natural bed depression evolution in nature [e.g., *Houtenbos*, 1998].

[18] We assume that the sediment transport can be described by a generalization of the empirical formula with a slope correction term added (equation (8)), so that the sediment is transported easier downhill than uphill. As $b > 1$, this formula expresses that transport depends in a nonlinear way on the flow velocity. In order to make the analysis as simple as possible the boundaries are considered infinitely far away, which applies to offshore situations.

[19] The equations are rewritten into a nondimensional form by defining

$$\begin{aligned}\mathbf{u}&=U\mathbf{u}_*,\quad \mathrm{x}=l_m\mathrm{x}_*,\quad t=\frac{t_*}{\sigma}\\ h&=Hh_*,\quad \zeta=\frac{Ul_m\sigma}{g}\zeta_*,\end{aligned} \tag{9}$$

in which U is the magnitude of the current and σ is the tidal frequency. The horizontal longitudinal scale is the tidal excursion length, i.e., half the maximum distance traveled by a water particle in one period: $l_m = U/\sigma$. By introducing this scaling into the original equations and the dispersion relation $L\sigma=\sqrt{gH}$ for a shallow water wave to determine the tidal wavelength L we arrive

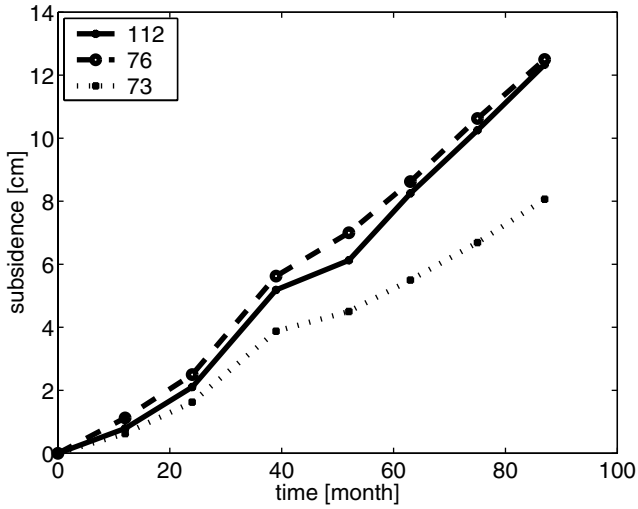

Figure 4. The local subsidence in time for measurement locations 112, 76, and 73. The horizontal axis denotes the time in months from October 1986, and the vertical axis denotes the absolute subsidence in centimeters. The data source is *Eysink et al.* [1995].

at the constituting equations (the asterisks are dropped for convenience):

$$\frac{\partial \zeta}{\partial x}+\frac{\partial u}{\partial t}+u\frac{\partial u}{\partial x}+v\frac{\partial u}{\partial y}-\hat{f}v+\frac{\hat{r}u}{1+\delta^2\zeta-h}=0, \qquad (10)$$

$$\frac{\partial \zeta}{\partial y}+\frac{\partial v}{\partial t}+u\frac{\partial v}{\partial x}+v\frac{\partial v}{\partial y}+\hat{f}u+\frac{\hat{r}v}{1+\delta^2\zeta-h}=0, \qquad (11)$$

$$\delta^2\frac{\partial \zeta}{\partial t}-\frac{\partial h}{\partial t}+\frac{\partial}{\partial x}\left[\left(1-h+\delta^2\zeta\right)u\right]+\frac{\partial}{\partial y}\left[\left(1-h+\delta^2\zeta\right)v\right]=0, \qquad (12)$$

$$\frac{\partial h}{\partial t}=-\hat{\alpha}\nabla\cdot|\mathbf{u}|^b\left(\frac{\mathbf{u}}{|\mathbf{u}|}-\hat{\lambda}\nabla h\right)-\hat{\rho}e^{-\hat{L}_f^2\left(x^2+y^2\right)}. \qquad (13)$$

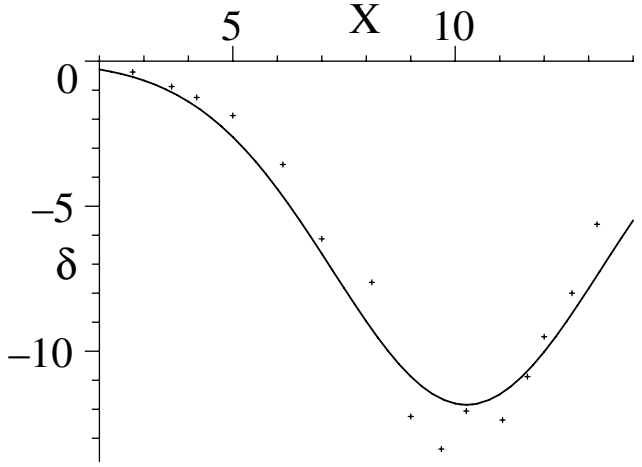

Figure 5. Approximation of the measured data of January 1994 (pluses) by a Gaussian curve (solid thick line). The horizontal axis is the rescaled distance as defined in Figure 3, and the vertical axis is the depression in centimeters.

The dimensionless parameters are defined in Table 2. The maximum tidal velocity U is of the order of 1 m s^{-1}. The frequency σ of the M_2 tide in the North Sea is 1.4×10^{-4} s^{-1}. This results in a value of about 7 km for l_m. The tidal wavelength is of the order of 700 km, which means that δ is small, $\delta \approx 0.01$. The linearized friction coefficient r can be estimated from the drag coefficient c_D [*Hulscher*, 1996]. The value for the drag coefficient c_D in a shallow sea lies between 0.01 and 0.001. The depth is assumed to be 30 m, which is a typical value for the southern part of the North Sea. Hence $\hat{r}$ lies between 0.24 and 2.4; here we use the default value $\hat{r} = 0.6$. The Coriolis parameter at 52°N is 1.16×10^{-4} s^{-1}; hence $\hat{f} = 0.8$. The exponent in the transport formula b is set at 3, and the slope factor λ is set equal to 2, following earlier similar work [*Hulscher et al.*, 1993]. The constant α can be computed from *Van Rijn* [1993] and is set at a value of 1.5×10^{-5} s^2 m^{-1}. However, *Roos and Hulscher* [2002] recently showed that α may well be a factor 10 larger because stirring of wind waves and human activities such as extensive fishing will shorten the morphological timescale by a factor 10 (see section 6). We will continue here with the "slowest" value. The depression radius R is 3000 m and the value of ρ is taken as 5.8×10^{-10} m s^{-1}, both based on the analysis of section 2. Table 2 gives the numerical values of the dimensionless parameters for the North Sea situation.

[20] T_m (see Table 2) is the morphological timescale for the inherent morphodynamic behavior, for example, the timescale of the growth of tidal sandbanks [see *Hulscher et al.*, 1993]. T_f (see Table 2) is a morphological-forcing timescale defined as the period that the forcing needs to create a subsidence equal to the water depth H = 30 m. As in the North Sea, T_m ($\simeq$ 450 years) and T_f ($\simeq$ 1600 years) are about the same size; interaction is likely. Note that the subsidence is a linear process and is therefore observable from the start.

[21] Since $T_m \simeq 450$ years (being the slowest value; the fastest would be 45 years) and $T_f \simeq 1600$ years, the bottom elevation will hardly change at the tidal time scale t, from which it is assumed that $\partial h/\partial t = 0$ in the hydrodynamic momentum and continuity equations. For the same reason the net, i.e., tidally averaged, sediment fluxes determine the slow evolution of the bed. Therefore a "slow" time variable $\tau = \hat{\alpha}t$ is substituted into equation (13) to yield

$$\frac{\partial h}{\partial \tau}=-\vec{\nabla}\cdot\left\langle|\mathbf{u}|^b\left[\frac{\mathbf{u}}{|\mathbf{u}|}-\hat{\lambda}\nabla h\right]\right\rangle-\mu e^{-\hat{L}_f^2\left(x^2+y^2\right)}. \qquad (14)$$

Here the angle brackets denote a tidal average and

$$\mu=\frac{\hat{\rho}}{\hat{\alpha}}=\frac{T_m}{T_f}=0.28. \qquad (15)$$

The parameter μ is the ratio of the morphological timescale T_m and the morphological forcing timescale T_f. It is smaller than 1, which enables solving the set of equations via an expansion in μ (see section 4). (If T_f had been smaller than the morphological timescale T_m, the slow time variable $\tau = \hat{\rho}t$ would have been substituted as a slow time variable. As a consequence, the factor μ would still have been smaller than 1 and allow for an expansion.)

Table 1. Values for the Maximum Subsidence δ_{max} and Radius R Using the Best Fit of the Gaussian Profile Model on the Measured Data at Ameland

Time	δ_{max}, cm	R, m
Feb. 1991	6.34	2954
Jan. 1992	8.12	3033
Jan. 1994	11.85	3022

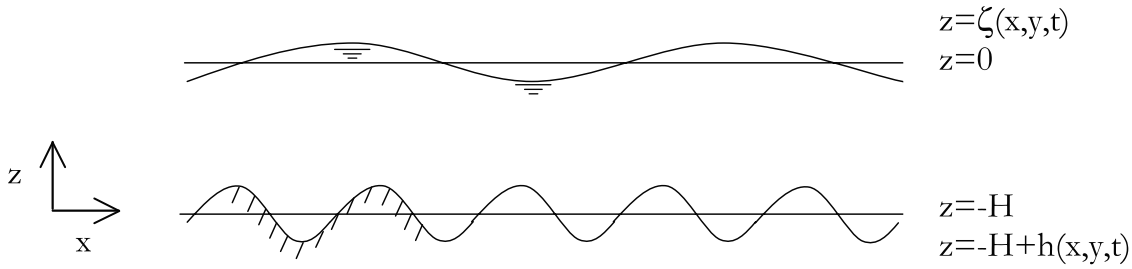

Figure 6. The model geometry (side view). The y axis is directed into the paper. Adapted from *Németh et al.* [2002].

[22] The averaging theorem guarantees that (14) is an approximation of the original bottom equation (13) at the morphological timescale [*Krol*, 1991]. To solve the evolution equation for h, we first have to determine the flow at the "fast" timescale. This is done by solving the flow equations (10), (11), and (12) with $\partial h/\partial t = 0$.

4. Solving the Bed Evolution

4.1. Zeroth-Order Solution

[23] The exact solution can symbolically be written as the vector $\psi = (u, v, \zeta, h)$. Since $\mu < 1$, we can expand the solution in a polynomial in μ:

$$\psi = \psi_0 + \mu\psi_1 + \mu^2\psi_2 + \ldots, \tag{16}$$

where ψ_0 corresponds to the zeroth-order solution, here describing a tidal flow over a horizontal bed, i.e., $\psi_0 = (u_0, v_0, \zeta_0, 0)$; ψ_1 denotes the first-order solution in μ, etc. Since, compared to μ, δ^2 is very small, namely $\cong 1 \times 10^{-4}$, it is assumed that the terms $\mathcal{O}(\delta^2)$ can be neglected. So u_0, v_0, and ζ_0 follow from

$$\frac{\partial \zeta_0}{\partial x} + \frac{\partial u_0}{\partial t} + u_0\frac{\partial u_0}{\partial x} + v_0\frac{\partial u_0}{\partial y} - \hat{f}v_0 + \hat{r}u_0 = 0, \tag{17}$$

$$\frac{\partial \zeta_0}{\partial y} + \frac{\partial v_0}{\partial t} + u_0\frac{\partial v_0}{\partial x} + v_0\frac{\partial v_0}{\partial y} - \hat{f}u_0 + \hat{r}v_0 = 0, \tag{18}$$

$$\frac{\partial u_0}{\partial x} + \frac{\partial v_0}{\partial y} = 0, \tag{19}$$

$$\frac{\partial}{\partial x}\left\langle |\vec{u}|^2 u_0 \right\rangle + \frac{\partial}{\partial y}\left\langle |\vec{u}|^2 v_0 \right\rangle = 0. \tag{20}$$

[24] A possible flow solution is

$$\hat{u}_0(t) \equiv C \quad \mathbf{v}_0(t) \equiv 0, \tag{21}$$

where C is a constant. The solution for ζ_0 is not further considered as it plays no role in the further analysis. The solution describes a spatially uniform, time-independent tide over a flat bed. One could object that this is inconsistent since no tidal frequency is involved in the case of uniform flow. However, earlier work has shown that the results of the stability analysis explaining tidal sandbanks are not essentially different for sinusoidal motion, an alternating block function or steady flow [*Huthnance*, 1982; *De Vriend*, 1988]. These equations can also be used to model morphologic evolution under an alternating block function (period $2\pi\sigma^{-1}$) representing tidal motion. Without presenting the full formal derivation we will implement this at the end of this section.

4.2. First-Order Solution

[25] Using the zeroth-order solution, the first-order solution ψ_1 follows from the following set of equations:

$$\frac{\partial \zeta_1}{\partial x} + C\frac{\partial u_1}{\partial x} - \hat{f}v_1 + \hat{r}(Ch_1 + u_1) = 0, \tag{22}$$

$$\frac{\partial \zeta_1}{\partial y} + C\frac{\partial v_1}{\partial x} + \hat{f}u_1 + \hat{r}v_1 = 0, \tag{23}$$

$$\frac{\partial u_1}{\partial x} + \frac{\partial v_1}{\partial y} - C\frac{\partial h_1}{\partial x} = 0, \tag{24}$$

$$\frac{\partial h_1}{\partial \tau} + \frac{\partial}{\partial x}\left[3C^2u_1 - C^3\hat{\lambda}\frac{\partial h_1}{\partial x}\right] + \frac{\partial}{\partial y}\left[C^2v_1 - C^3\hat{\lambda}\frac{\partial h_1}{\partial y}\right] + e^{-\hat{L}_f^2\left(x^2+y^2\right)} = 0. \tag{25}$$

If the radius of the bottom depression were zero, the value of L_f would become infinite, which implies that the exponent term in (24) would vanish. In this case the model exactly coincides with the set of equations describing the inherent (linear) morphodynamic instability at the scale of sandbanks. This problem without subsidence has been investigated by several authors [cf. *Huthnance*, 1982; *De Vriend*, 1988; *Hulscher et al.*, 1993].

[26] In order to derive a closed evolution equation for h_1 we will first solve u_1, v_1 and ζ_1 as a function of h_1 in (22), (23), and (24). The unknowns are Fourier-transformed as follows:

$$\begin{aligned} u_1 &= \int\int \tilde{u}_1(\mathbf{k}, t)e^{-i\mathbf{k}\cdot\mathbf{x}}d\mathbf{k} + \text{c.c.}, \\ v_1 &= \int\int \tilde{v}_1(\mathbf{k}, t)e^{-i\mathbf{k}\cdot\mathbf{x}}d\mathbf{k} + \text{c.c.}, \end{aligned} \tag{26}$$

Table 2. Definitions and Numerical Values of the Main Dimensionless Model Parameters for a Typical North Sea Situation

Parameter	Definition	North Sea Value
δ	$\frac{l_m}{L}$	0.01
$\hat{f}$	$\frac{f}{\sigma}$	0.8
$\hat{r}$	$\frac{r}{\sigma H}$	0.6
$\hat{\lambda}$	$\lambda\frac{H\sigma}{U}$	8.4×10^{-3}
$\hat{\alpha}$	$\frac{\alpha U^b}{Hl_m\sigma} = \frac{1}{\sigma T_m}$	5×10^{-7}
$\hat{\rho}$	$\frac{\rho}{H\sigma} = \frac{1}{\sigma T_f}$	139×10^{-7}
$\hat{L}_f$	$\frac{l_m}{\sqrt{2R}}$	1.68

$$\zeta_1 = \int\int \tilde{\zeta}_1(\mathbf{k},t)e^{-i\mathbf{k}\cdot\mathbf{x}}d\mathbf{k} + \text{c.c.},$$
$$h_1 = \int\int \tilde{h}_1(\mathbf{k},t)e^{-i\mathbf{k}\cdot\mathbf{x}}d\mathbf{k} + \text{c.c.}, \quad (27)$$

in which $i^2 = -1$, c.c. means complex conjugate, and $\mathbf{k} = (k, l)$ is a two-dimensional wave number vector. This transformation is based on the fact that the bottom topography in an infinite domain can be uniquely decomposed into a spectrum of wave components, so that integration over all these wave components exactly equals the bed topography. The function $\tilde{h}$ $(\mathbf{k}, t)$ can be regarded as the amplitude function of a wave with wave vector components (k, l).

[27] In general, the subsidence center of subsidence is arbitrary with respect to the phase of the bed topography. We now examine the case in which the bed subsidence center coincides with a sandbank trough and in which no rhythmic topography is present at the onset of the bed subsidence. This leads to the following Fourier transformation of the forcing term in (25):

$$e^{-\hat{L}_f^2\mathrm{x}^2} = \int\int -\frac{1}{4\pi\hat{L}_f^2}e^{-\frac{k^2+l^2}{4\hat{L}_f^2}}e^{-i\mathbf{k}\cdot\mathbf{x}}d\mathbf{k} + \text{c.c.}. \quad (28)$$

Equations (22), (23), and (24) can now be written as

$$\begin{bmatrix} -ik & \hat{r}-Cik & -\hat{f} \\ -il & \hat{f} & \hat{r}-Cik \\ 0 & -ik & -il \end{bmatrix}\begin{bmatrix} \tilde{\zeta}_1 \\ \tilde{u}_1 \\ \tilde{v}_1 \end{bmatrix} = \tilde{h}_1\begin{bmatrix} -\hat{r}C \\ 0 \\ -Cik \end{bmatrix} \quad (29)$$

The determinant of the matrix is nonzero, so there is a unique solution for $\tilde{\zeta}_1$, $\tilde{u}_1$, and $\tilde{v}_1$. The solutions for the velocities $\tilde{u}_1$ and $\tilde{v}_1$ are

$$\tilde{u}_1 = \tilde{h}_1 C\frac{(l^2-k^2)\hat{r} - k\hat{f}\,l + ik^3C}{-\hat{r}(k^2+l^2) + ik^3C + il^2kC} \quad (30)$$

$$\tilde{v}_1 = \tilde{h}_1 C\frac{k\left(\hat{f}\,k - 2l\hat{r} + ilkC\right)}{-\hat{r}(k^2+l^2) + ik^3C + il^2kC}. \quad (31)$$

This result can be substituted into (25) to arrive at

$$\frac{\partial\tilde{h}_1}{\partial\tau} - \hat{\omega}\tilde{h}_1 - \frac{1}{4\pi\hat{L}_f^2}e^{-\frac{k^2+l^2}{4\hat{L}_f^2}} = 0, \quad (32)$$

with

$$\hat{\omega} = C^3\left[\frac{ik\left(l^2\hat{r} - 3k^2\hat{r} + 3ik^3C - 2kl\hat{f} + ikl^2C\right)}{(ikC-\hat{r})(k^2+l^2)} - \hat{\lambda}\left(k^2+l^2\right)\right].$$

The parameter $\hat{\omega}$ is a complex frequency; its real part denotes the amplification $(Re(\hat{\omega}) > 0)$ or decay $(Re(\hat{\omega}) < 0)]$ rate and its imaginary part denotes the phase migration speed. A detailed explanation is presented by *Németh et al.* [2002]. When tidal motion is modeled as an alternating block function, the imaginary part of $\hat{\omega}$ becomes exactly zero (no migration), and the real part of $\hat{\omega}$ equals its value found for the uniform, time-independent current. Therefore we find

$$\omega = Re(\hat{\omega}) = C^3\left[2\frac{\left(l\hat{r} - k\hat{f}\right)k^2lC}{(\hat{r}^2 + C^2k^2)(k^2+l^2)} - \hat{\lambda}\left(k^2+l^2\right)\right]. \quad (33)$$

Solving (31) yields the first-order solution

$$\tilde{h}_1(k,l,\tau) = \hat{h}_i e^{\omega\tau} - \frac{1}{4\pi\hat{L}_f^2}\frac{(1-e^{\omega\tau})}{\omega}e^{-\frac{k^2+l^2}{4\hat{L}_f^2}}, \quad (34)$$

where $\hat{h}_i$ is the (initial) amplitude of the large-scale rhythmic features, i.e., tidal sandbanks that are present at the start of gas mining. In principle, $\hat{h}_i$ can be a function of the wave vector components k, l. The fact that a similar parameter $\hat{\omega}$ shows up in this approximation procedure makes clear that the natural morphodynamics (eigenmodes) of the system play an important role in the bed evolution when the bed is forced because of gas mining. The combined zeroth- and first-order solution of the bed evolution reads

$$\tilde{h}(k,l,\tau) = \tilde{h}_0 + \mu\tilde{h}_1 = h_i e^{\omega\tau} - \frac{\mu}{4\pi\hat{L}_f^2}\frac{(1-e^{\omega\tau})}{\omega}e^{-\frac{k^2+l^2}{4\hat{L}_f^2}}. \quad (35)$$

5. Bed Evolution Results

5.1. System Without Gas Mining

[28] A subsidence speed of zero ($\mu = 0$), or assuming that $\hat{L}_f$ in (34) is infinite, refers to natural morphological behavior in which the evolution $\tilde{h}(k, l, \tau)$ of initially small-amplitude modes yields $\tilde{h}(k, l, \tau) = h_i e^{\omega\tau}$. Choosing $\tilde{h}_i$ wave number-independent leads to the linear stability problem investigated extensively by various authors [*Huthnance*, 1982; *De Vriend*, 1988; *Hulscher et al.*, 1993], who presented results for the growth rate ω only. In order to achieve a similar presentation as for the results for gas extraction we need contour plots of $\tilde{h}$. We also set the initial amplitude h_i at 0.01 so that the evolution results are the same size as for the case with gas mining. In physical terms this means that all large-scale rhythmic features are initially present and have an amplitude of 0.3 m, much smaller than the amplitude of observed tidal sandbanks.

[29] Figure 7 shows contours of $\tilde{h}$ at $\tau = 1$ for all possible combinations of wave number k along the x axis and wave number l along the y axis. (Note that wave numbers of $K \sim 10$ and larger cannot be modeled properly with this 2DH model as for these scales, vertical motion should be incorporated [*Hulscher*, 1996].) The contour plot is limited to the half plane of k ($k > 0$) as Figure 7 is point symmetrical in the origin $(k, l) = (0,0)$.

[30] The ratio between the wave number components expresses the orientation of the bed mode with the dimensionless wave number K, defined as $K = \sqrt{k^2+l^2}$. The physical wave characteristics are the actual wavelength λ_w and angle ϕ, defined as the angle between the principal current direction and the crests in clockwise direction, both given by

$$\lambda_w = \frac{2\pi U}{K\sigma} \qquad \phi = \arctan\frac{k}{l}. \quad (36)$$

[31] The dominant, most amplified ($\omega \approx 1.33$), mode at $\tau = 1$ is $(k, l) = (2.0, -3.2)$, which corresponds to an actual wavelength of 11.9 km and wave crests oriented at 32° counterclockwise relative to the principal current direction. The most amplified mode is time-independent, which means that this mode always dominates for small bed amplitudes. These results compare reasonably well with the observed scales and orientations of tidal ridges in shallow seas [*Off*, 1963; *Huntley et al.*, 1993].

[32] In line with the findings of *Huthnance* [1982] and *Hulscher et al.* [1993] we would like to have quantitative information on the influence of the Coriolis force on this mode. If the Coriolis force is zero, the contours (Figure 8) are symmetrical about the x axis. The two dominating modes, $(k, l) = (1.4, \pm 3.7)$, correspond to $\omega =$

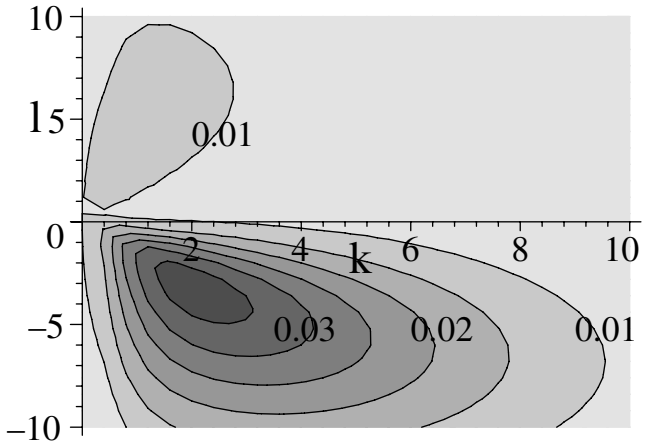

Figure 7. Contour plot of the value of $\tilde{h}$ at $\tau = 1$ by a uniform flow $C = 1$ m s^{-1}. The initial amplitude h_i is set at 0.01. Parameter setting: $\hat{f} = 0.8$, $\hat{r} = 0.6$, and $\hat{\lambda} = 8.4 \times 10^{-3}$.

0.76. Thus the growth rate ω is reduced by almost a factor 2. The actual wavelength of these modes is 11.3 km, which is only slightly smaller than in the case with Coriolis force. The wave crests have a preferred direction of about 21°. This means that the Coriolis force causes anticlockwise orientation of the tidal sandbanks in the Northern Hemisphere. Weak Coriolis forces result in instabilities because of resistance. Being nonrealistic, low-resistance cases fall outside the scope of this study.

[33] We also want to quantify the influence of another important factor, the current velocity magnitude C. Increases in C lead to a faster than linear increase in ω, as can be seen in (33). Table 3 gives an impression of the impact of the velocity value C on the maximum growth rate ω, the corresponding morphological time T_{ms} (defined as the period after which an initial amplitude has increased by a factor e^1), wave number K, and angle ϕ. The wave number K decreases, which implies that the actual wavelength increases as the velocity increases. This effect is even stronger in dimensional terms, which take changes in the morphological length scale l_m into account.

5.2. System With Gas Mining

[34] The evolution (34) refers to the system in which the bed evolves because of both sediment movement and gas mining. We start modeling at the beginning of mining, i.e., $\tau_0 = 0$, and we assume that there are no initial bed forms present: $h_i = 0$ for all k, l. The evolution for the gas mining case is presented in a contour plot

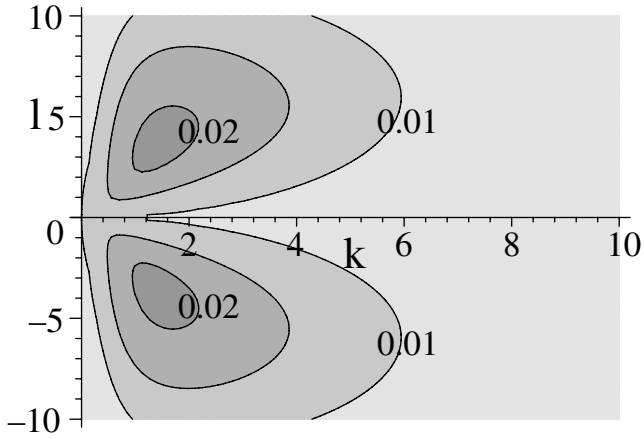

Figure 8. A contour plot of $\tilde{h}$ at $\tau = 1$ by a uniform flow $C = 1$ m s^{-1} without Coriolis forces. Other parameters are as in Figure 7.

Table 3. Maximum Value of ω and Its Corresponding Significant Morphological Time T_{ms}, the Wave Number K and Angle ϕ for Various Values of the Current Velocity C[a]

C, m s^{-1}	Maximum ω	K	ϕ	T_{ms}, year
0.5	0.31	6.1	−34°	$\simeq 1.45 \times 10^3$
1.0	1.33	3.8	−32°	$\simeq$338
1.5	3.10	2.8	−32°	$\simeq$1.45
2.0	5.61	2.3	−31°	$\simeq$80

[a] The parameters $\hat{r}$, $\hat{f}$, and $\hat{\lambda}$ are equal to the values given in Figure 7.

of $\tilde{h}$ for all physical relevant combinations of k and l in Figure 9a. The dominant mode corresponds to the combination (k, l) with the largest value for $\tilde{h}$ at time $\tau = 1$. Please note that in this case the dominant mode itself also varies with time.

[35] The maximum value of $\tilde{h}$ at $\tau = 1$ is obtained by the wave vector $(k, l) = (1, -1)$; here $\tilde{h}(1, -1) = 0.0113$. This suggests that at that moment the dominant mode in the bed pattern has a very large wavelength and a preferred direction of 45° counterclockwise with respect to the principal current. Figure 9b corresponds to the evolution of the bottom depression only, i.e., when the flow is below the threshold value for sediment transport. In that case the largest amplitude at $\tau = 1$ is found at the origin: $\tilde{h}(0, 0) = 0.0078$. The amplitude of the dominant mode is ~45% larger in the combined case. This implies that two types of bed behavior, forced and natural, enhance each other.

[36] The temporal evolution of the bottom is shown in Figure 10 giving contour plots of $\tilde{h}$ at increasing time τ. Correspondingly, Table 4 shows the numerical values for the maximum $\tilde{h}$ and its corresponding wave number K and orientation ϕ for the combined system of natural and human-induced forcing. For comparison, the maximum value of $\tilde{h}$ of the corresponding bed evolution below the threshold value for sediment transport is given. Note that the only difference between this no-sediment transport case and Figure 9b is a factor that increases with time; the maximum value is always found in the origin, which means that there is no preferred direction.

[37] As time increases, the wave number of the dominant mode increases from $K = 0.8$ to $K = 1.8$. The amplitude values $\tilde{h}$ are larger than those found when neglecting sediment transport. The difference in bed amplitude is 45% at $\tau = 1$ and increases to 190% at $\tau = 2$. The influence of the sediment transport must cause this faster growth.

6. Discussion

[38] Comparing the results of the natural system with the combined system (Figures 9a and 10), we find essential differences in bed evolution in cases with and without a bottom depression. In the former case, initial (infinitesimal) perturbations are necessary to form a wavy bed: the initially most amplified mode is the dominant one. This dominant mode, $K = 3.8$, is time-independent and corresponds to an actual wavelength of 11.9 km. The crests are rotated 32° counterclockwise with respect to the current. In the case of gas mining, no initial amplitude is necessary to allow topographic changes. Here the largest-amplitude mode is time-dependent. For $\tau = 1$ the largest amplitude belongs to a mode with wave number $K = 1.4$ and orientation 45°, counterclockwise with respect to the current. For the theoretical limiting case of infinite time, i.e., $\tau \to \infty$ where $\tau > 10$, we find that the dominant mode approaches the mode found for the system without gas mining. Hence the induced depression changes the natural behavior (a flat seabed would remain unchanged), and similarities in evolution (preferred orientation and large time limit) express the strong connections with natural seabed behavior.

[39] If the direct results of the dead, i.e., without sediment transport, subsidence system (Figure 9b) are compared with those of the live system of subsidence and morphodynamics (Figure 9a), we observe significant differences. The dead system has a Gaus-

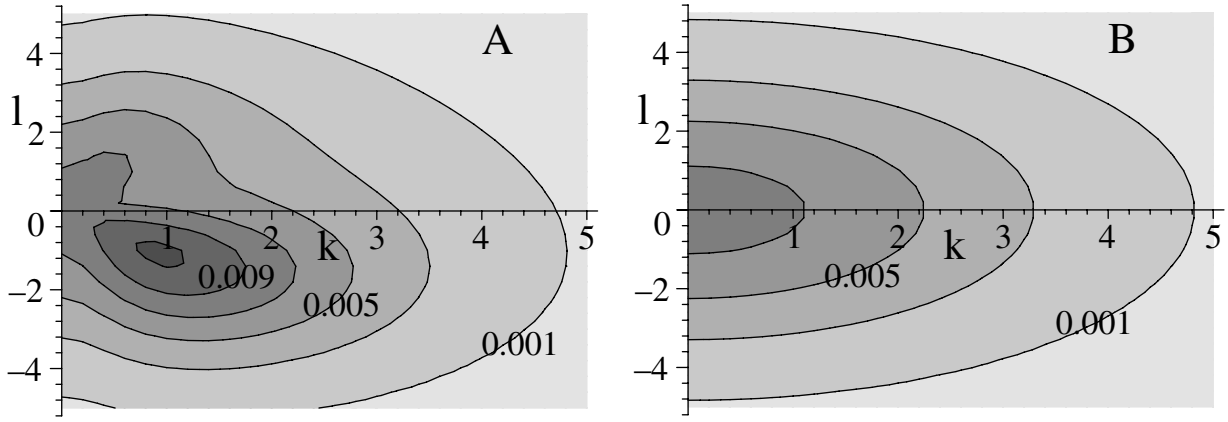

Figure 9. A contour plot of $\tilde{h}$ at $\tau = 1$ for different values of k and l for the combined system (a) including sediment transport and (b) bed subsidence only, without sediment transport.

sian shape, and the contours in the horizontal (k, l) plane are always circles since at each time level, the amount of subsidence exclusively depends on the distance to the center of the depression. This symmetry is broken when sediment transport is allowed, as can be observed in its state at $\tau = 1$ (Figure 9a). We observe a clear immediate preference for counterclockwise orientations with respect to the current, a growing relative difference between the largest amplitude and that of its surrounding modes, and a gradual shift of the dominant mode from zero at $\tau = 0$ toward a tidal sandbank mode, which would be reached after a long time.

[40] From the distribution of the Fourier-transformed bed contours we observe that for the live system the energy is more

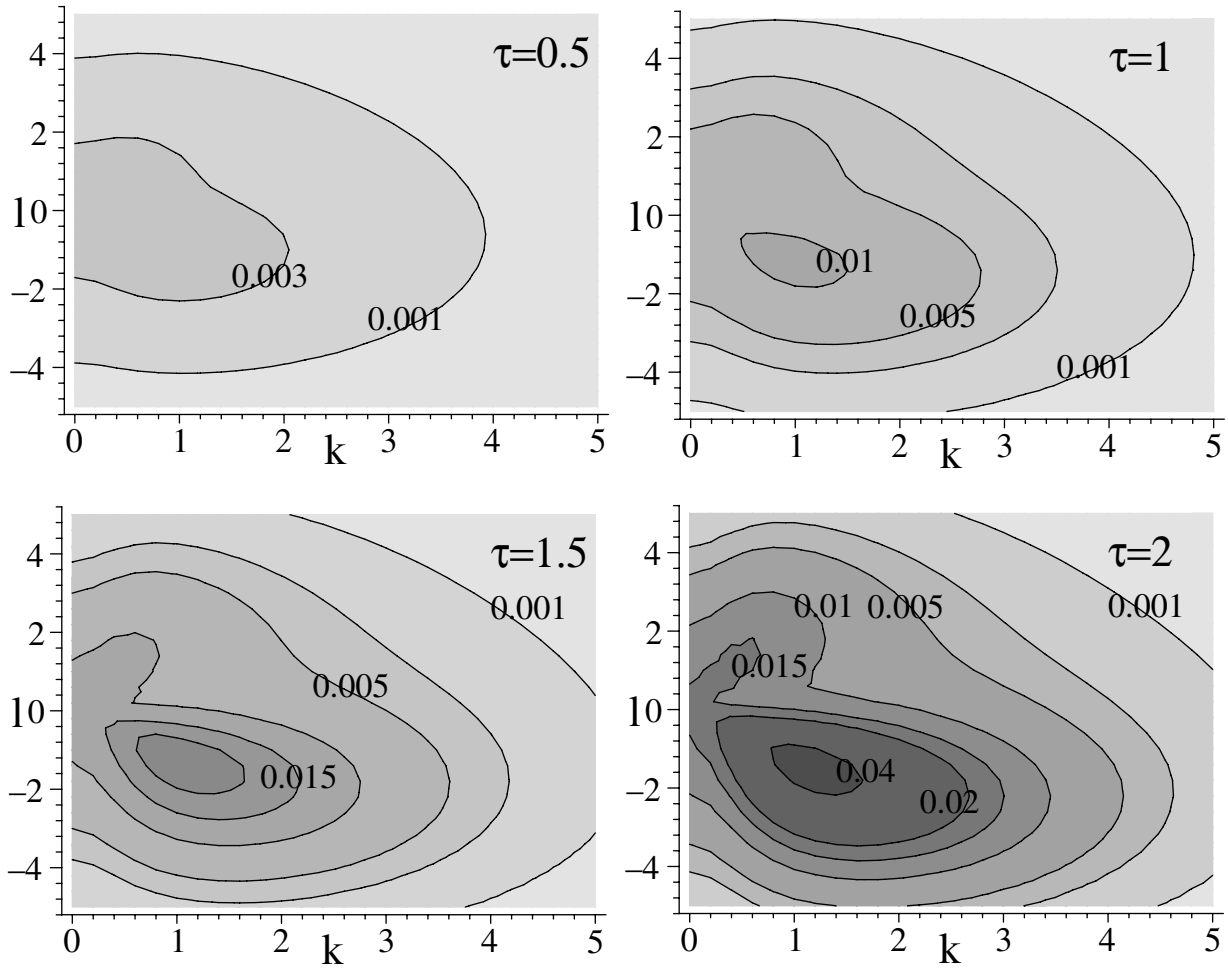

Figure 10. A contour plot of $\tilde{h}$ for different values of k and l as τ increases when $h_i = 0$. Other parameters are as in Figure 8. The contours correspond to $\tilde{h}$ levels of 0.001, 0.003, 0.005, 0.01, 0.015, 0.02, 0.025, 0.03, 0.035, and 0.04, respectively. Please note their nonlinear distribution.

Table 4. Maximum Value of $\tilde{h}$ and the Corresponding Wave Number K and Angle ϕ for Various Time Levels τ When the Morphodynamics are Excluded and Included, Respectively[a]

	Morphodynamics Excluded	Morphodynamics Included			Effect of
τ	Maximum $\tilde{h}$	K	ϕ	Maximum $\tilde{h}$	Morphodynamics
0.5	0.0039	0.8	−45°	0.0044	+13%
1.0	0.0078	1.4	−45°	0.0113	+45%
1.5	0.0117	1.8	−40°	0.0234	+99%
2.0	0.0157	1.8	−40°	0.0456	+190%

[a] Also the effect of the morphodynamics (defined as relative increase of $\tilde{h}$ due to morphodynamics with respect to its corresponding amplitude in the no-sediment transport case) is given.

concentrated in a certain part of the spectrum around the dominant mode (Figure 9a) than for the dead system (Figure 9b). This indicates that in the morphodynamic case the influence of the depression may well reach beyond the initial depression area. For comparison, note that in theory a single mode in Fourier space corresponds to an infinite sinusoidal pattern in (x, y) space. As this concentration becomes stronger in time (Figure 10), it may imply that the influenced zone expands with time. In physical terms it may lead to the initiation of tidal-sandbank-like features besides the stretched original depression. These can induce adjacent troughs again. This process would make the original depression a trigger and center for bed pattern formation. This matter is explored by *Roos and Hulscher* [2002].

7. Conclusions and Final Remarks

[41] In this study the evolution and morphological consequences of marine gas mining have been investigated using a mathematical approximation method: expansion in the small parameter μ. Unlike the models used so far, this model explicitly includes the effect of sediment transport. The analysis shows that the morphological evolution of the bottom is more complex than the sum of natural behavior and undisturbed subsidence.

[42] The analysis explicitly reveals differences between the bed evolution with and without sediment transport. These differences are caused by interaction between bed subsidence and large-scale bed features, which are, in fact, the eigenmodes of the system. The most important varying physical parameters are the Coriolis force and the current velocity. As a consequence of combined evolution, the maximum depth of the subsidence-induced depression increases by 45% after one morphological timescale (because of uncertainty in the sediment transport value, this period lies between 45 and 450 years) for parameters representing a typical North Sea case. The main subsidence axis becomes oriented at 45° anticlockwise with respect to the current direction. This is close to the orientation of tidal sandbanks in tidal seas (30°[cf. *Huthnance*, 1982]). Clearly, there are substantial differences between the evolution of a subsidence-induced depression below(dead bed) and above (live bed) the threshold value. The latter is attained for strong tidal currents, as present, for example, in the Southern North Sea. The intermediate (10–100 years) and long-term effects of subsidence of the sea bottom can only be predicted by taking into account the interaction between the natural morphodynamics and the forced response due to the subsidence.

[43] The linear analysis is based on a small perturbation on a flat bed. This can be regarded as a first step toward an investigation of a realistic perturbation in a fully developed seabed. The latter may be a flat bed or a bank-patterned-bed, depending on the stability properties within this model. Stable configurations are supposed to be realized in nature. However, growth toward such a stable configuration takes a long time for sandbanks so that the study of human perturbations starting from an unstable equilibrium does not necessarily contradict reality. In that case, natural and human-related perturbations may grow simultaneously. A nonlinear sandbank analysis will show the validity of this linear analysis. This knowledge is also needed for the study of the long-term impact of human actions: interactions between human perturbation and intrinsic behavior are expected. This aspect is left for future research.

[44] The method used in this paper, i.e., approximation in a small parameter, can be applied to other morphodynamic cases in which human interference and natural bed development coexist. Such situations are common: sand extraction pits and/or artificial sand deposits (initial value problems) and dredging of a navigation channel. The dynamical behavior will differ from what is found in this model as those kinds of human interference have different temporal structures compared with continuous bed subsidence.

[45] **Acknowledgments.** The useful discussions and helpful comments of Huib De Vriend are gratefully acknowledged. The authors thank Trijnie Maurer-van Dijk for the electronic data transfer, which helped us create Figure 3, and Michiel Knaapen and Attila Németh for their help in making the figures. This work was performed within the EU-sponsored project Human Interaction With Large-Scale Coastal Morphologic Evolution (HUMOR) EVK3-CT-2000-00037 and was cosponsored by the Technology Foundation STW, the applied science division of NWO, and the technology program of the Dutch Ministry of Economic Affairs.

References

Allen, J. R. L., *Current Ripples, Their Relation to Patterns of Water and sediment Motion*, 433 pp., North-Holland, New York, 1968.

De Vriend, H. J., Inherent stability of depth-integrated mathematical models of coastal morphology, paper presented at Symposium on Mathematical Modelling of Sediment Transport in the Coastal Zone, Int. Assoc. of Hydraul. Res., Copenhagen, Den., 1988.

Dyer, K. R., and D. A. Huntley, The origin, classification and modelling of sandbanks and ridges, *Cont. Shelf Res.*, *19*, 1285–1330, 1999.

Eysink, W. D., N. Dankers, K. S. Dijkema, H. F. van Dobben, C. J. Smit, and J. de Vlas, Monitoring effects of bottom subsidence at the eastern part of the Island Ameland: First evaluation after eight years of gasdrilling (in Dutch), *Delft Hydraul. Rep. H841*, Delft, Neth., 1995.

Fluit, C. C. J. M., A morphological model for a marine bottom subsidence influenced by tide-topography interactions, M.S. thesis, Univ. of Twente, Enschede, Neth., 1999.

Houtenbos, A. P. E. M., Bottom depression Ameland 1986–1998 (in Dutch), *NAM Topogr. Dep. Rep. 199803000426*, Ned. Aardolie Maatschappij, Assen, Neth., 1998.

Hulscher, S. J. M. H., Tidal-induced large-scale regular bed form patterns in a three-dimensional shallow water model, *J. Geophys. Res.*, *101*, 20,727–20,744, 1996.

Hulscher, S. J. M. H., and G. M. van den Brink, Comparison between predicted and observed sand waves and sandbanks in the North Sea, *J. Geophys. Res*, *106*, 9327–9338, 2001.

Hulscher, S. J. M. H., H. E. de Swart, and H. J. de Vriend, The generation of offshore tidal sandbanks and sand waves, *Cont. Shelf. Res.*, *13*, 1183–1204, 1993.

Huntley, D. A., J. M. Huthnance, M. B. Collins, C.-L. Lui, R. J. Nicholls, and C. Hewitson, Hydrodynamics and sediment dynamics of North Sea sand waves and sandbanks, *Philos. Trans. R. Soc. London, Part A*, *343*, 461–474, 1993.

Huthnance, J., On one mechanism forming linear sandbanks, *Estuarine Coastal Shelf Sci.*, *14*, 79–99, 1982.

Knaapen, M. A. F., S. J. M. H. Hulscher, H. J. De Vriend, and A. Stolk, A new type of seabed waves, *Geophys. Res. Lett.*, *28*, 1323–1326, 2001.

Komarova, N. L., and S. J. M. H. Hulscher, Linear instability mechanisms for sand wave formation, *J. Fluid Mech.*, *413*, 219–246, 2000.

Krol, M., On a Galerkin-averaging method for weakly nonlinear wave equations, *Math. Appl. Sci.*, *11*, 649–664, 1991.

Németh, A. A., S. J. M. H. Hulscher, and H. J. de Vriend, Modelling migration of sand waves in shallow shelf seas, *Cont. Shelf Res.*, in press, 2002.

Off, T., Rhythmic linear sand bodies caused by tidal currents, *AAPG Bull.*, *47*, 324–341, 1963.

Peck, R. B., Deep excavations and tunnelling in soft ground, paper presented at 7th International Conference in Soil Mechanics and Foundation Engineering, Soil Mech. Found., Mexico City, 1969.

Roos, P. C., and S. J. M. H. Hulscher, Formation of offshore tidal sand banks triggered by a gasmined bed subsidence, *Cont. Shelf Res.*, in press, 2002.

Van Alphen, J. S. L. J., and M. A. Damoiseaux, A geomorphological map of the Dutch shoreface and adjacent part of the continental shelf, *Geol. Mijnbouw*, *68*, 433–444, 1989.

Van Rijn, L. C., *Handbook of Sediment Transport by Currents and Waves*, Aqua, Amsterdam, 1993.

Zimmerman, J. T. F., Vorticity transfer by tidal currents over an irregular topography, *J. Mar. Res.*, *38*, 601–630, 1980.

C. C. J. M. Fluit and S. J. M. H. Hulscher, Department of Civil Engineering, University of Twente, P.O. Box 217, 7500 AE Enschede, Netherlands. (s.j.m.h.hulscher@ctw.utwente.nl)

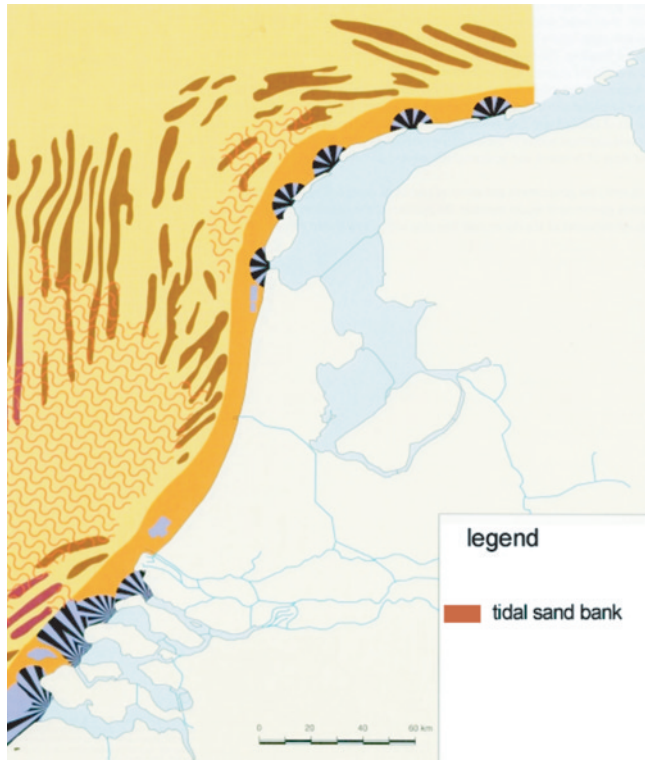

Figure 1. Location of tidal sandbanks and sand waves in the North Sea. Adapted after *Van Alphen and Damoiseaux* [1989].